

Automated detection of malignant features in confocal microscopy on superficial spreading melanoma versus nevi

Dan Gareau

Oregon Health and Science University
Department of Dermatology
and
Department of Biomedical Engineering
3303 Southwest Bond Avenue
Portland, Oregon 97239
and
Memorial Sloan-Kettering Cancer Center
Dermatology Service
160 East 53rd Street
New York, New York 10022

Ricky Hennessy

Oregon Health and Science University
Department of Biomedical Engineering
3303 Southwest Bond Avenue
Portland, Oregon 97239

Eric Wan

Oregon Health and Science University
Department of Biomedical Engineering
3303 Southwest Bond Avenue
Portland, Oregon 97239

Giovanni Pellacani

University of Modena and Reggio Emilia
Department of Dermatology
Via del Pozzo 71
Modena 41100, Italy

Steven L. Jacques

Oregon Health and Science University
Department of Dermatology
and
Department of Biomedical Engineering
3303 Southwest Bond Avenue
Portland, Oregon 97239

1 Introduction

Superficial spreading melanoma (SSM) is the most fatal form of skin cancer and the most common lethal skin cancer, with an estimated mortality rate of 14%.¹ The incidence of melanoma in the United States is 60,000 new cases each year, increasing 2% per year.¹

Melanomas are thought to originate (*in-situ* melanoma) in the epidermis near the dermal-epidermal junction (DEJ), causing disarray, and progress in lateral and then vertical (invasive melanoma) growth phases leading to metastasis and death.² The current methods of treating melanoma are: standard surgical

Abstract. *In-vivo* reflectance confocal microscopy (RCM) shows promise for the early detection of superficial spreading melanoma (SSM). RCM of SSM shows pagetoid melanocytes (PMs) in the epidermis and disarray at the dermal-epidermal junction (DEJ), which are automatically quantified with a computer algorithm that locates depth of the most superficial pigmented surface [$D_{SPS}(x,y)$] containing PMs in the epidermis and pigmented basal cells near the DEJ. The algorithm uses 200 noninvasive confocal optical sections that image the superficial 200 μm of ten skin sites: five unequivocal SSMs and five nevi. The pattern recognition algorithm automatically identifies PMs in all five SSMs and finds none in the nevi. A large mean gradient ψ (roughness) between laterally adjacent points on $D_{SPS}(x,y)$ identifies DEJ disruption in SSM $\psi = 11.7 \pm 3.7 [-]$ for $n = 5$ SSMs versus a small $\psi = 5.5 \pm 1.0 [-]$ for $n = 5$ nevi (significance, $p = 0.0035$). Quantitative endpoint metrics for malignant characteristics make digital RCM data an attractive diagnostic asset for pathologists, augmenting studies thus far, which have relied largely on visual assessment. © 2010 Society of Photo-Optical Instrumentation Engineers. [DOI: 10.1117/1.3524301]

Keywords: melanoma; melanin; confocal microscopy; computer vision; pathology detection.

Paper 10093SSRR received Feb. 24, 2010; revised manuscript received Oct. 18, 2010; accepted for publication Oct. 21, 2010; published online Dec. 28, 2010.

excisions, chemotherapy, radiation therapy, and immunotherapy, which offer various degrees of success. The National Cancer Institute (Bethesda, Maryland) estimates the overall five-year survival rate for melanoma to be 90.5%, with percentages ranging from 97.6% (localized stage 1 to 2) to 16.2% (stage 4).³ Because of the tendency for melanoma to metastasize, detection of *in-situ* melanoma is critical for efficient excision. We present a technique to quantify traits of indolent² melanoma *in situ* (stage 1 to 2) prior to invasion based on two criteria: 1. the presence of single melanoma cells in the epidermis called pagetoid melanocytes (PMs), and 2. DEJ disarray (high-spatial-frequency fluctuations in the DEJ). These diagnostics involve tissue no deeper than the basal layer, which is within the

Address all correspondence to: Dan Gareau, Oregon Health and Science University, Department of Dermatology, Mail code: CH16D, 3303 SW Bond Ave., Portland, OR 97329. Tel: 503-708-7078; E-mail: gareaud@ohsu.edu.

penetration limit ($\sim 250 \mu\text{m}$) of confocal microscopy using 830-nm laser light.

Diagnostic guidance for surgical treatment of melanoma has improved from the early standard of care protocol by Handley in 1905: a 5-cm marginal excision.⁴ Improved histopathology enabled prognostic indicators such as Clark's level staging in 1969, which classified the general stages (1 to 4) of melanoma progression. The Breslow thickness measurement⁵ achieved greater reproducibility by quantifying the depth of invasion from the skin surface. Toward earlier diagnosis with better prognosis, new diagnostic techniques are emerging. The next major milestone may be quantitative, noninvasive imaging of microscopic features focusing on *in-situ* diagnosis in superficial regions, to avoid treating late-stage disease. 70% of *in-situ* melanoma is SSM with associated pagetoid spread (presence of PMs), 15% is lentigo maligna melanoma with associated DEJ disarray, and 15% shows mixed characteristics. However, virtually all *in situ* has irregularity in the pigmented network of the epidermis⁶ and the diagnostically relevant basal and granular layers are superficial regions noninvasively accessible with reflectance confocal microscopy (RCM). At this shallow depth, where melanomas arise in nevi whose pigment provides contrast to observe normal/abnormal morphology, there is interest to classify the superficial pigmented cell networks as nevoid or melanoma. Shadowing is not a concern, because it is extremely rare for primary melanoma to arise in the dermis without involving the basal or granular layers of the epidermis.⁶

Clinical dermatologists identify suspected melanoma by eye with the aid of the dermoscope⁷ (lacks cellular resolution) to then biopsy, so well-trained pathologists can achieve high sensitivity/specificity. There is a clinical need for noninvasive confocal microscopy and automated computer pathology as a buffer between visual inspection and biopsy.

RCM using 830-nm laser light enables noninvasive axial optical sectioning of 1 to 2 μm and lateral resolution of 0.5 μm .⁸ RCM complements imaging modalities such as magnetic resonance imaging,⁹ optical coherence tomography,¹⁰ and high-frequency ultrasound,¹¹ with the particular strength of high resolution. High NA optical coherence tomography (OCT) is essentially the same as RCM, but with lower noise due to its use of a coherence gate to further reject multiply scattered light, although both OCT and RCM suffer from aberrations (a limiting factor for imaging at depth). Currently available OCT sources allow ~ 1 -to-2- μm axial resolution, therefore the method of this work could be implemented using high-resolution focus-tracked OCT.

Like physical sectioning in routine histopathology, the optical sectioning capability of RCM shows microscopic features of normal skin.^{12,13} Due to highly refractive melanin granules (diameter = 43 nm¹⁴ and refractive index of $n = 1.72$ ¹⁵) in epidermis ($n = 1.34$ ¹⁶), melanin provides strong contrast in pigmented cells using RCM.¹⁷ RCM is an imaging modality suited well for imaging both benign and malignant epidermal melanocytic morphology *in vivo*.¹⁸ RCM acquisition "stacks" sequentially captured optical sections at various depths in skin. Penetration of 250 μm (or at least up to the first concentrated pigment) reaches the papillary and superficial reticular dermis,¹⁹ enabling noninvasive diagnostic survey of the more superficial basal layer.

Pathological evaluation in RCM images has so far included only characterization by the human eye. Though RCM is

attractively more volumetrically inclusive than feasible histology, human scanning of large confocal volumetric data is time consuming. This job may be best suited for computer automation, presuming reliable quantitative features can be automatically identified. Reproducible terminology, such as the suggested descriptive traits useful for the human reviewer,²⁰ must be quantified in computer vision for unequivocal melanoma, and may be even more attractive in challenging cases such as Spitz nevi.²¹

Current techniques for noninvasive computer-automated melanoma detection, based on macroscopic imaging (i.e., non-cellular detail) such as polarized dermoscopy^{22,23} in combination with the Melafind algorithm,^{24,25} have thus far achieved only modest specificity with adequate sensitivity. These techniques are only slightly better than other (macroscopic imaging) automated diagnostics of cancer in the breast and lung. The sensitivity for dermoscopy, using the human eye with two common logic algorithms (CASH or ABCD rule), is reportedly as high as 98% with specificity ranging from 70 to 90%.²⁶ Though automated computer algorithms have shown good concordance with human classification,²⁷ in low-resolution dermoscopy, automated analysis with confocal images of microscopic structures shows greater promise. Accurate diagnostics requiring cellular resolution have enabled automated cytopathology in Papanicolaou test analysis.^{28,29} The goal of this work is to provide similar quantitative metrics from confocal images of skin. This work focuses two metrics that can aid the clinician in diagnosing SSM with high-resolution image analysis software: 1. the number of PMs present, and 2. the roughness of the superficial pigmented basal layer near the DEJ.

PMs occur in SSM (the predominant subgroup *in-situ* melanoma in the lateral growth phase) and are defined as melanocytes abnormally located above the basal layer in the epidermis, which sometimes form nests.^{30,31} PMs are detectable in both conventional histopathology and RCM.^{32,33} The presence of roundish PMs in the epidermis between the stratum corneum and the basal layer up to 100 μm deep has a sensitivity of 77.9% and a specificity of 81.4% for indicating melanoma.³³ This lateral growth phase precedes the vertical growth phase when the melanoma invades the basement membrane, leading to deadly metastasis, so SSM with PMs is an ideal target for early detection.² However, not all SSMs have PMs, and the overall roughness characteristic of the DEJ surface is another relevant pathological aspect. The breakdown of the DEJ, termed "nonedged papillae" due to the appearance of a broken DEJ as sectioned by RCM in *en-face* images, has been reported 89.7% sensitive and 58.6% specific.³³

The algorithm presented here isolates the depth location of the most superficial pigmented surface $D_{\text{SPS}}(x,y)$, which is the most strongly reflective voxel (along z) at each x - y location. The diagnostically important DEJ can be approximately marked, located, and visualized by $D_{\text{SPS}}(x,y)$ due to a step function in melanin concentration from the epidermis to the basal layer in all skin types. $D_{\text{SPS}}(x,y)$ can be reliably located because penetration to and beneath $D_{\text{SPS}}(x,y)$ are not issues: the epidermis does not strongly attenuate, and deeply invading melanoma (i.e., prognostic information) always displays the superficial atypia. In isolating $D_{\text{SPS}}(x,y)$, the stratum corneum, nonpigmented epidermis, and deeper dermis are digitally removed to reveal the diagnostically important pigmented cell network either above

(in the case of PMs) or in the basal layer. PMs appear as discreet, cell-sized elevations >1 cell width above the basal layer in $D_{\text{SPS}}(x,y)$. The roughness of $D_{\text{SPS}}(x,y)$, which is a diagnostic measure that correlates with the overall breakdown of the DEJ, is not very sensitive to PMs, since PMs occupy only a small lateral fraction of $D_{\text{SPS}}(x,y)$.

2 Materials and Methods

2.1 Patients and Confocal Imaging

Patients with SSM, imaged at the University of Modena and Reggio Emilia, Italy, gave informed consent for RCM prior to biopsy during routine screening. The SSM group (two Fitzpatrick type-2 skin lesions and three type-3 lesions) contained (histologically) one apparently without PMs, two with subtle PMs, and two with obvious PMs. Imaging was performed on a region containing visually recognizable pagetoid cells and DEJ disarray, and the SSMs were prescreened by coauthor and expert confocal pathologist Pellacani to select only lesions containing both PMs and junctional involvement.

RCM, reviewed by coauthor Pellacani, showed unequivocal normal morphology for the dermoscopically normal control lesions, suggesting four junctional lentiginous nevi, or “jentigo,” and one congenital nevus. The four jentigo subjects were imaged at Lucid Incorporated, Rochester, New York, and consisted of clinically unsuspecting nevi with a low level of asymmetry, low border irregularity, uniform color distribution, and small diameter. The congenital nevus had a known static history since birth and was imaged voluntarily by coauthor Gareau at Sloan Kettering Cancer Center, New York, New York. All locations had the same equipment with the same settings.

For each site, a single axial stack was acquired with the VivaScope 1500TM (Lucid Incorporated, Rochester, New York, operating at 830-nm wavelength). After each image capture, the *en-face* optical section (500- μm field of view) was translated 1 μm deeper along the optical axis into the tissue from above the surface of the skin to beneath the maximum depth of optical penetration where the images were dark. The 1- μm axial step size was chosen because the axial resolution at the 830-nm wavelength is about 2 μm ; therefore 1- μm steps satisfied the Nyquist sampling criteria: two samples per resolution element. The step and capture routine was repeated 200 times over 1 min, collecting 200 8-bit .bmp images (1024 \times 1024 pixels, 300-MB total memory space). To avoid saturation and account for optical attenuation deep in the stack, the laser power was continuously and automatically adjusted for each optical section to match the 256 gray-level range of pixels to the dynamic range of the imaging system.

2.2 Machine Vision Algorithm

The algorithm, created using MatLab 7.8TM (MathWorks, Natick, Massachusetts), consisted of three preprocessing subroutines.

1. Confocal optical sections were loaded into a contiguous volume matrix. Due to natural patient movement during clinical imaging, the optical sections were generally not aligned laterally, and had an x - y -shift for each successively deeper image in each stack.

2. A multidimensional unconstrained nonlinear minimization (Nelder-Mead) minimized the difference between axially adjacent optical sections to determine proper coregistration lateral offset values, eliminating motion artifact. Our coregistration routine, available online,³⁴ was of similar speed to the comparable routine “Auto-Blend Layers” in Photoshop (Adobe, San Jose, California) on a standard MacBook Pro (Macintosh, Cupertino, California), but was optimized for large stacks. The severity of the correction depended on the microscope stability during clinical acquisition, but in general, the total lateral displacement was not more than 20% of the 500- μm field of view. Of the ten datasets involved in this study, nine were successfully realigned and one dataset was discarded due to a 40% lateral movement, so an eleventh dataset (replacement control nevus) was included to complete the study.
3. 3-D images were adjusted for the field curvature of the RCM (about 10 μm in 500- μm FOV). At each x,y position, the depth-resolved reflected signal $R(z)$ was analyzed to find the superficial peak at the water-coupled interface between stratum corneum and the imaging window at $z = z_0$. An adjusted 3-D image was generated, which was coregistered relative to the surface: $R(z') = R(z - z_0)$. Hence, this last preprocessing subroutine shifted each column of voxels in the image axially, such that optical sections in the adjusted 3-D image represented a flat x - y plane in the tissue. At each depth z' , the values of $R(x,y)$ were normalized by the mean value $\langle R(x,y) \rangle$, to equalize the image $R(x,y,z') = R(x,y,z') / \langle R(x,y,z') \rangle$ causing areas with high reflectivity to stand out.

After preprocessing, a topographical map $D_{\text{SPS}}(x,y)$ [μm] was isolated that specified the position of the most reflective voxel along z' at each x,y position. $D_{\text{SPS}}(x,y)$ located the superficial pigmented basal cells (or melanocytes) resting on the DEJ and the occasional PM.

The “roughness” of $D_{\text{SPS}}(x,y)$ was computed as the mean spatial gradient of $D_{\text{SPS}}(x,y)$. The absolute gradient in the x direction ($G_x = |dD_{\text{SPS}}/dx|$) and the absolute gradient in the y direction ($G_y = |dD_{\text{SPS}}/dy|$) were added [Eq. (1)] to create a gradient map (G) of $D_{\text{SPS}}(x,y)$ with a mean of: roughness ψ [Eq. (2)] with units of axial microns per lateral micron on $D_{\text{SPS}}(x,y)$, a unitless quantity that describes $D_{\text{SPS}}(x,y)$ irregularity.

$$G = \sqrt{G_x^2 + G_y^2}, \quad (1)$$

$$\psi = \frac{1}{n} \sum_1^n G_i. \quad (2)$$

2.3 Absolute Reflectance

To convert from measured laboratory units the photodetector output volts to true reflectivity from the focus, the data, after correction for adjusted laser power, were multiplied by a calibration constant C ,

$$C = R_{gw} / V_{gw}, \quad (3)$$

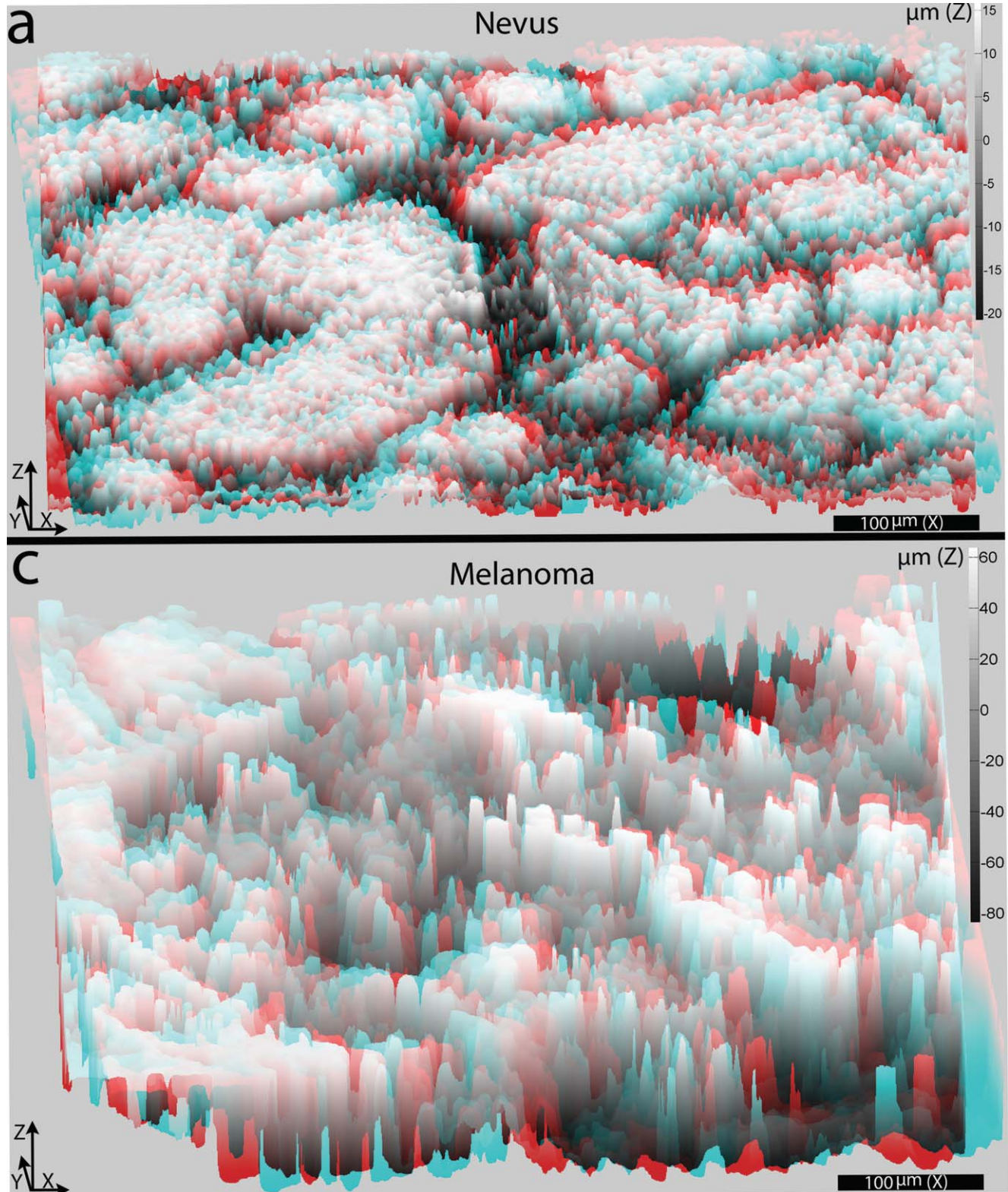


Fig. 1 $D_{SPS}(x,y)$ of nevi (a,b) and superficial spreading melanoma (c,d) veiwed at 30 deg with respect to the skin surface plane (anaglyphic 3-D, 4-deg azimuthal separation of red/cyan left/right aspects). Video (a) shows junctional lentiginous nevus with basal nests. Video (b) shows a congenital nevus with intradermal component. Video (c) and video (d) show a superficial spreading melanomas with heavy pagetoid component. For illustration, the Z scale bars (to right of images) quantify axial position deviation from the mean of $D_{SPS}(x,y)$. For proper veiwing, use 3-D glasses from the insert. For the viewing online, e-mail the corresponding author for an extra pair of 3-D glasses by mail if necessary. (Video (a), QuickTime, 6.1 MB [URL: <http://dx.doi.org/10.1117/1.3524301.1>]; Video (b), QuickTime, 6.1 MB [URL: <http://dx.doi.org/10.1117/1.3524301.2>]; Video (c), QuickTime, 6.1 MB [URL: <http://dx.doi.org/10.1117/1.3524301.3>]; Video (d), QuickTime, 6.1MB [URL: <http://dx.doi.org/10.1117/1.3524301.4>].)

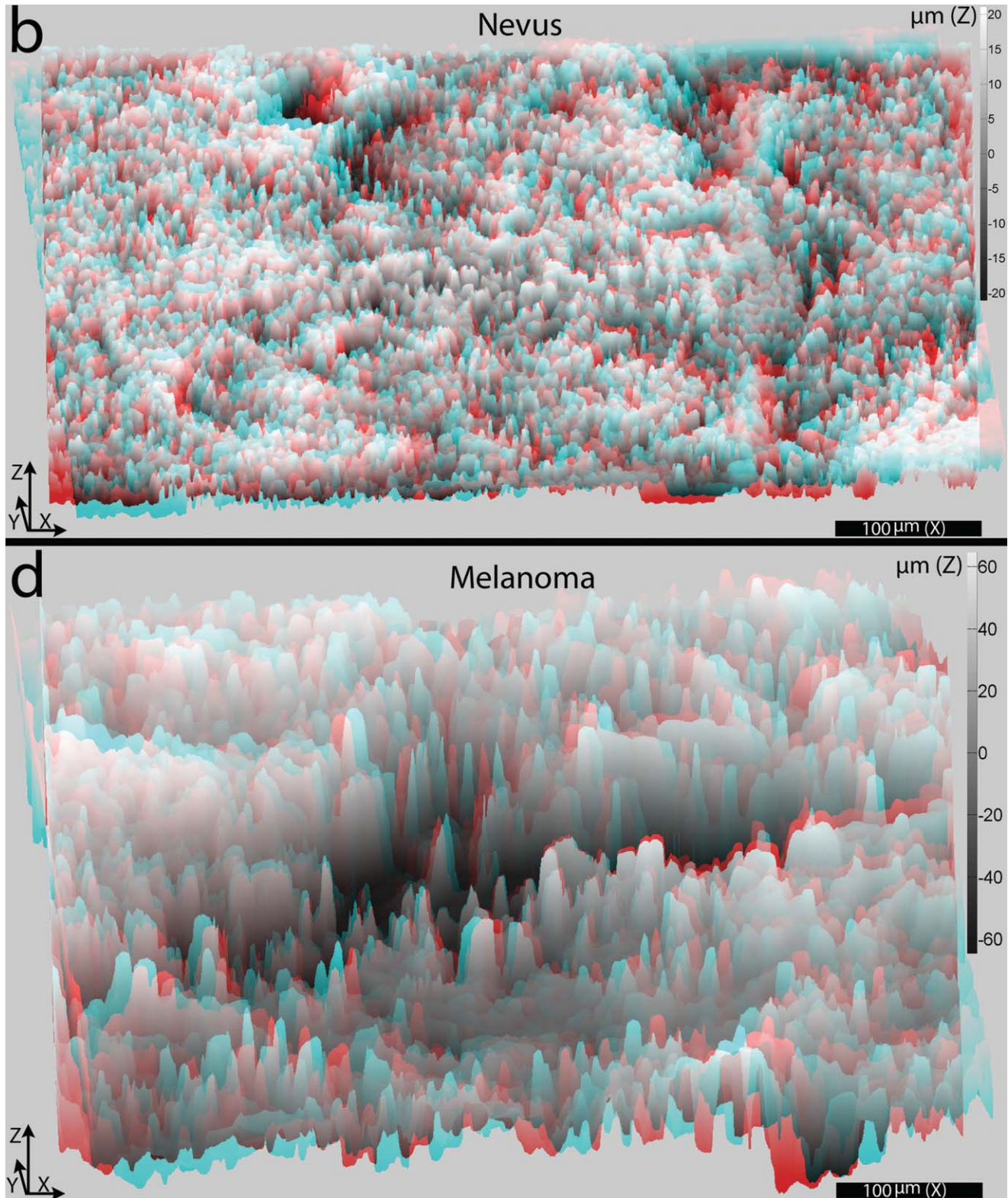


Fig. 1 (continued)

where R_{gw} was the theoretically computed reflectance at the glass/water sample interface, $R_{gw} = [(n_g - n_w)/(n_g + n_w)]^2$, and V_{gw} was the measured signal [V] measured when focused on the interface. In practice, glass ($n = 1.52$) or polycarbonate ($n = 1.58$) can be used with crodomol oil

($n = 1.46$) or water ($n = 1.33$), yielding $R_{gw} = 0.00444$, $R_{gc} = 0.00405$, $R_{pw} = 0.00738$, or $R_{pc} = 0.00156$. Though not critical for feature analysis, true reflectivity units illustrate endogenous tissue reflectance for comparison among studies.

Table 1 Roughness factors $\psi = \langle G \rangle$ [Eq. (1)], where G is the gradient [Eq. (2)] for five nevi and five superficial spreading melanomas.

Nevi	SSM	Legend
6.1226*	9.7760&	* = congenital nevus
5.8304#	17.6942!	# = jentigo
4.4148#	10.9738!	\$ = subtle SSM
4.4414#	7.87260\$	& = mid-grade SSM
6.6186#	12.0322&	! = obvious SSM

2.4 Detecting Pagetoid Melanocytes

PMs were identified in the reflectance data on the $D_{SPS}(x,y)$ by shallow depth, large gradients of reflectance, and $D_{SPS}(x,y)$ surrounding the cell, and a small circumference-to-area ratio typical of roundish PMs (a term used in Ref. 33). Locations on $D_{SPS}(x,y)$ were identified as PMs with the following thresholds chosen by cross-validation.

1. They were located at a depth between 20 and 100 μm beneath the glass window interface. Rationale: PMs occur in the superficial epidermis.
2. The ratio of their reflectance (based on contiguous high reflectance segmentation to identify border) to the reflectance 3 μm outside their border, and G [Eq. (1)] at the border, were both greater than 1.7. Rationale: surrounding epidermal keratinocytes are comparatively nonreflective and PMs should present discreet elevations in $D_{SPS}(x,y)$.
3. Their area was at least 144 μm^2 . Rationale: excludes stray melanin flecks.
4. Their perimeter was less than 175 μm . Rationale: excludes dendritic type cells, selecting only roundish PMs.

3 Results

Disruption of the $D_{SPS}(x,y)$ exhibited a high roughness factor for SSM ($\psi = 11.7 \pm 3.7, n = 5$), (mean \pm SD), whereas the $D_{SPS}(x,y)$ displayed a low roughness factor for nevi ($\psi = 5.5 \pm 1.0, n = 5$). The two populations were entirely separable (see Table 1). A 1-tailed t-test for two sample sets of unequal variance yielded $p = 0.0035$. Figure 1 shows samples of $D_{SPS}(x,y)$ for nevi versus SSMs.

3.1 Pagetoid Melanocyte Detection

Applying the threshold algorithm identified PMs in all the SSMs but not in any of the nevi. Figure 2 shows an example of the true reflectivity versus depth for a trace (axial profile) through a single PM. Compared to the true reflectance of 0.00023 previously reported for a mouse melanocyte at 488 nm,³² the human PM shown at $z \approx 30$ to 60 μm appears 3.5 times more reflective at 830 nm, $R_M = 0.00080$.

For each SSM, a set of two to three tissue sites ($60 \times 60 \times 60$ voxels = $30 \times 30 \times 60 \mu\text{m}$) were identified that either contained a clearly visible PM or contained only normal epidermal cells (NEC). Figure 3 shows examples of PMs and NECs.

A histogram of the true reflectivity [see Eq. (3)] of the 108,000 voxels in each cell cube was generated. A clear normal distribution of low reflectivity voxels was apparent (associated with background epidermal reflectivity) and was fit with a Gaussian distribution (mean \pm SD = 15 ± 5 ($n \approx 90,000$ voxels) [counts] for both PM and NEC sites (a histogram, N_{low} versus $\text{COUNTS}_{\text{low}}$). Then this background was subtracted from the histograms, yielding a difference distribution of $\sim 20,000$ voxels with higher reflectivity (a histogram, N_{high} versus $\text{COUNTS}_{\text{high}}$). The integration of the product $N_{\text{low}} \text{COUNTS}_{\text{low}}$ and the product $N_{\text{high}} \text{COUNTS}_{\text{high}}$ yielded the total reflected counts from low reflectivity voxels (C_{low}) and high reflectivity voxels (C_{high}), respectively. The ratio $C_{\text{high}}/C_{\text{low}}$ was used to characterize the site for the presence or absence of a PM, and also served to cancel any site-to-site variation in strength of reflectance.

A range of threshold values of $C_{\text{high}}/C_{\text{low}}$ was tested for the ability to properly discriminate 12 PM and 12 NEC, yielding the plot of sensitivity (S_e) versus specificity (plotted as $1-S_p$) in Fig. 4. The figure shows that S_e equals S_p at a value of 0.74. As the threshold is lowered, S_e rises and S_p drops. S_e equals 0.96 when S_p equals 0.50. Other analysis methods for discriminating PM from NEC are being tested, but this preliminary study illustrates the potential for a simple metric to detect PMs.

3.2 Confocal Features and the $D_{SPS}(x,y)$

Confocal raw and processed $D_{SPS}(x,y)$ images are shown *en-face*, perpendicular to the typical histological sagittal sections, to demonstrate the lateral resolution within the confocal optical section, which is finer than the axial resolution. Figure 5(a) shows a SSM image with a lone PM indicated (same PM as profiled in Fig. 2). Figure 5(b) shows the corresponding $D_{SPS}(x,y)$ with the same pagetoid melanocyte indicated. The SSM is a Spitzoid melanoma from a 47-year-old female on the left leg (Breslow thickness 1.40 mm, Clark level 4, no ulceration, no

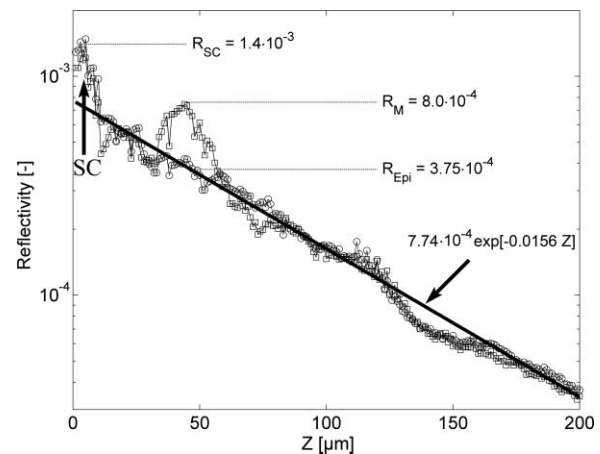


Fig. 2 Axial true reflectivity profile through one pagetoid melanocyte (squares), relative to a profile through laterally adjacent surrounding epidermis-only (circles). Centered at $z = 5 \mu\text{m}$, the reflectance of the stratum corneum (SC) is 1.4×10^{-3} . Beneath the SC, the bulk tissue reflectance decay is fit with an exponential. Centered at $z = 45 \mu\text{m}$, a pagetoid melanocyte's measured peak reflectance is 8.0×10^{-4} which is 4.25×10^{-4} above the epidermal background at $z = 45 \mu\text{m}$ (3.75×10^{-5}). The decaying exponential least square error fit to the data, which is not sensitive to data points in the SC ($z < 10 \mu\text{m}$), represents the background reflectance of the epidermis.

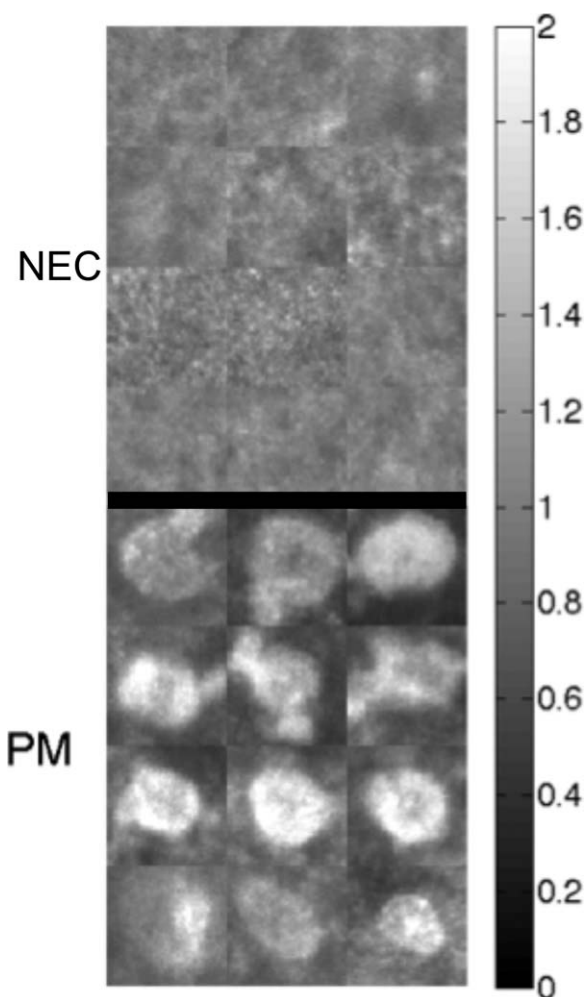


Fig. 3 *In-vivo* confocal reflectance images of 12 sites of normal epidermal cells (NEC) and 12 pagetoid melanocytes. Each image is the summation of voxel counts over the 30- μm depth distance of the image cube; then the image is normalized by the median value of all pixels. This normalization adjusts for site-to-site variations in the strength of the reflected signal, for example, when a site is more superficial or deeper in the skin.

regression). Relative to the skin surface, the depth of the pagetoid melanocyte is 40 μm , while the average depth of the surrounding $D_{\text{SPS}}(x,y)$ is $100 \pm 15 \mu\text{m}$. The correlating histology [Fig. 5(c)] does not show any pagetoid cells because of sparse physical sections in the sample of sparse pagetoid spread.

Figure 6 shows PM detection in the superficial spreading melanoma [Figs. 6(a), 6(b), and 6(c), see also Fig. 1(d)] from a 65-year-old female on the left back (Breslow thickness 0.69 mm, Clark level 3, no ulceration, no regression). $D_{\text{SPS}}(x,y)$ [Fig. 6(b)] shows rectangles that automatically located seven PMs. A single raw optical section [Fig. 6(c)] shows six of the PMs identified manually (arrows shown for reference). Comparatively, the nevus [Figs. 6(d) and 6(e), see also Fig. 1(a)] shows a smooth $D_{\text{SPS}}(x,y)$ and no automatically located PMs.

4 Discussion

RCM enables noninvasive cytological analysis to complement dermoscopy and histopathology for melanoma detection with

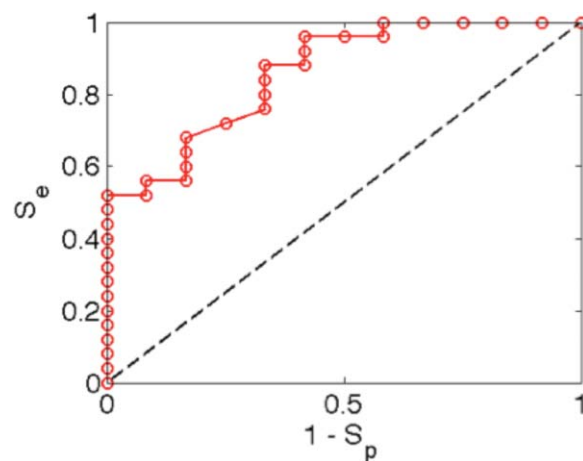


Fig. 4 Sensitivity (S_e) and specificity (S_p) of discriminating pagetoid melanocytes versus normal epidermal cells using the ratio $C_{\text{high}}/C_{\text{low}}$ as a discriminator, where C_{high} is the total reflectance from high reflectivity voxels and C_{low} is the total reflectance from low reflectivity voxels, within a $60 \times 60 \times 30\text{-}\mu\text{m}$ cube enclosing a suspected pagetoid melanocyte.

subcellular resolution and sufficient penetration to interrogate the dermal/epidermal junction where melanoma originates. However, RCM interpretation remains challenging, because digital grayscale data are unfamiliar to conventionally trained pathologists. Furthermore, large 3-D datasets are cumbersome to review. Automated isolation of the diagnostically valuable basal layer and identification of irregularity therein may expedite clinical translation of RCM from the bench to the bedside with 3-D graphics, facilitating the recognition of at least two

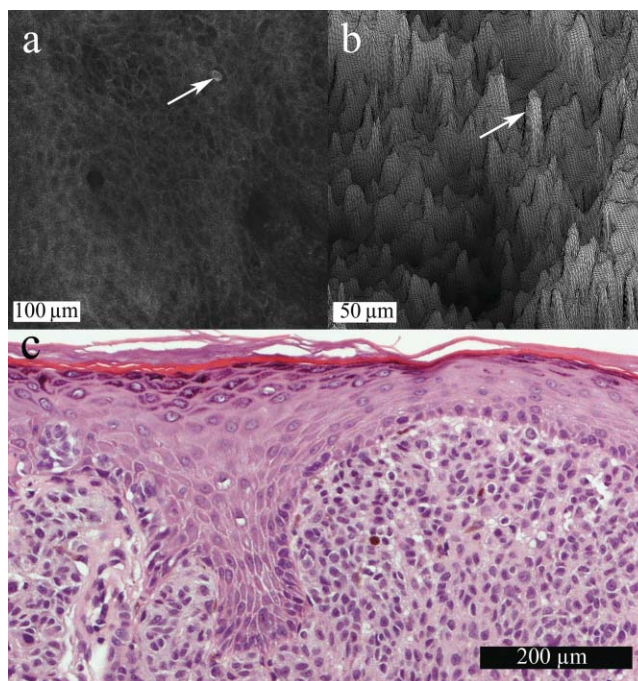


Fig. 5 Subtle superficial spreading melanoma. (a) A single optical section with a lone pagetoid melanocyte marked. (b) A 3-D surface plot of $D_{\text{SPS}}(x,y)$ viewed at 45 deg (same pagetoid melanocyte manually marked). (c) The correlating histology in standard sagittal view.

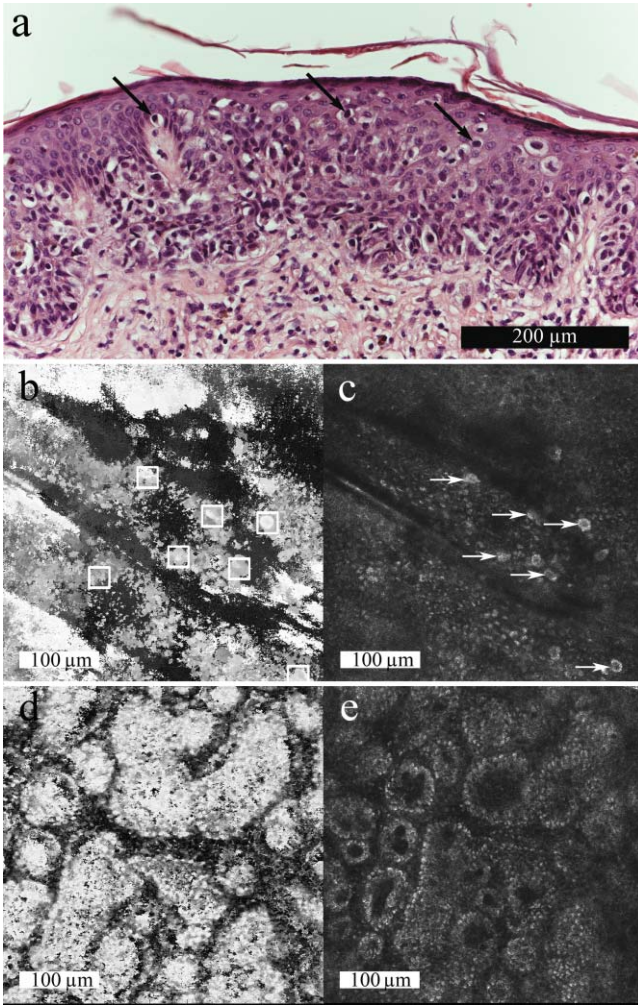


Fig. 6 (a) Histology of superficial spreading melanoma with clear pagetoid melanocytes (arrows). (b) Correlating $D_{SPS}(x,y)$ shown *en face*: bright pixels represent a more superficial $D_{SPS}(x,y)$. Pagetoid melanocytes are automatically marked (white squares) by the algorithm. (c) A sample optical section $50\ \mu\text{m}$ beneath the surface of the stratum corneum where pagetoid melanocytes are manually marked (arrows). (d) $D_{SPS}(x,y)$ for a junctional nevus where no pagetoid melanocytes are automatically identified. (e) A sample optical section at $35\ \mu\text{m}$ beneath the surface of the stratum corneum in the basal layer where normal pigmented basal cells show bright contrast.

many known RCM features³³ of melanoma, PMs, and DEJ disruption described by ψ [Eq. (2)].^{32,33}

The key discriminator used to detect PMs versus surrounding epidermis is high relative reflectivity due to increased melanin granule content, and possibly increased density of lipid membranes, which may even allow discrimination of amelanotic PMs. This latter possible mechanism of scatter awaits further study. Previous studies showing bright contrast of melanocytes in amelanotic melanoma suggest that contrast may arise from nonmelanized melanosomes that are 0.6 to $1.2\ \mu\text{m}$ and/or clinically unapparent melanin in premelanosomes.^{35,36} Though the mechanism of contrast is melanosomes ($0.7 \times 0.3\ \mu\text{m}$),³⁷ one important limitation of PM detection is the failure to differentiate pagetoid melanocytes from other pagetoid cells, in particular Langerhans cells, a notoriously difficult distinction with RCM, since they appear similar to pagetoid melanocytes.³⁸

Multispectral,³⁹ photoacoustic,⁴⁰ and/or angular resolved³⁹ microscopy show promise to specify Langerhans cells by identifying backscattering from Birbeck granules versus melanin granules in PMs.

$D_{SPS}(x,y)$ is dominated by basal cells and not PMs, since PMs occupy only a small portion of the lateral field of view. The small extent to which PMs do contribute to ψ remains under study. PMs lie on $D_{SPS}(x,y)$, and the interplay between the two is that PMs represent subsections of $D_{SPS}(x,y)$ with diagnostic interest of special importance and recognized melanocytes that are distinct from basal architecture.

Rather than addressing sensitivity/specificity for the technique, this feasibility work on nevi (no PMs as verified with expert visual RCM inspection by coauthor Pellcani) or SSM with various PM involvement, which serves only as proof of principal for automated discrimination of two visually known RCM melanoma features, may illustrate (see Fig. 5) one advantage of 3-D imaging: a single PM was found by the RCM algorithm and none were seen in the histology, which suffered from sampling error. More complete spatial coverage in both RCM and histology are required to fully explore and compare these two diagnostic techniques.

Studies underway include a ten-fold larger dataset with SSM, lentigo maligna, Clark's (dysplastic) nevi, and junctional lentiginous nevi, double-blinded to correlate histopathology for all cases. PM presence and large ψ are expected to vary for all subgroups, because, for example, in chronically sun-exposed Caucasian skin, 50 to 80 years of age, 70% of melanomas are lentigo maligna and may not involve PMs at all.⁶

Automated identification of the DEJ on types one, two, and three nonlesional skin is complex, involving multivariate regression analysis.⁴¹ While studies show promise across skin types and on nonlesional skin, our method only addresses differentiation of pigmented nevi versus SSM, a common task and appropriate target for these preliminary studies toward diagnosis of early SSMs that are very superficial (*in situ*) and challenging to dermoscopy. Furthermore, although the method presented here has not been investigated for Fitzpatrick skin type 1, Negroid, or Mongolian (types four, five, and six) skin, melanin is always preferentially concentrated in the basal layer.⁴² Since there are no significant differences in the number of melanocytes across the skin types, and total melanin content is thought to be governed by the rate at which melanocytes produce and distribute melanin,⁴² it seems a reasonable assumption that the relative contrast between hypomelanotic epidermis and hypermelanotic basal layer simply scales with skin type, enabling the contrast that consistently locates $D_{SPS}(x,y)$, with the possible caveat of insufficient optical penetration due to undegraded epidermal melanosomes in type four, five, and six skin. Caucasian keratinocytes exhibit greater melanin degradation, relatively,⁴³ but the effect is expected to be small.

Automated detection of melanoma may bridge the gap between dermoscopy (clinical) and biopsy (pathological), potentially offering greater accuracy than the former diagnostic without the difficulty of the latter. Unnecessary biopsy can be avoided, and more total lesions can be rapidly evaluated. The noninvasive approach may enable the detection of melanomas in remote environments without access to dermatologists. In summary, this pilot study applies digital quantification to (so far, human-based) malignant classification, increasing the

impact of RCM as a pathological tool. The dataset can be found on-line.³⁴

Acknowledgments

The authors would like to thank Milind Rajadhyaksha and Jay Eastman for establishing critical infrastructure; dermatologists Ashfaq Marghoob, Alan Halpern, and Alon Scope for clinical perspective on theoretical development of this work; and Billy Huang for collaboration in the early stages of this work. Dan Gareau is supported by an NIH National Research Service Award (NIH 5-T32-CA106195, PI: Molly Kulesz-Martin).

References

1. A. Jemal, R. Siegel, E. Ward, T. Murray, J. Xu, and M. J. Thun, "Cancer statistics," *CA Cancer. J. Clin.* **57**, 43–66 (2007).
2. D. Guerry, M. Synnstedt, D. E. Elder, and D. Schlutz, "Lessons from tumor progression: the invasive radial growth phase of melanoma is common, incapable of metastasis, and indolent," *J. Invest. Dermatol.* **100**(3), 342S–345S (1993).
3. Five year survival rates, retrieved 4 Aug. 2009, from Seer's training web site: see <http://training.seer.cancer.gov/melanoma/intro/survival.html>.
4. D. J. Eedy, "Surgical treatment of melanoma," *Brit. J. Dermatol.* **149**(1), 2–12 (2003).
5. A. Breslow, "Thickness, cross-sectional areas and depth of invasion in the prognosis of cutaneous melanoma," *Ann. Surg.* **172**, 902–908 (1970).
6. A. Solomon, Private communication, Oregon Health and Science Univ., Portland, OR (June 2010).
7. W. Stolz, U. Semmelmayr, K. Johow, and W. H. C. Burgdorf, "Principles of dermatoscopy of pigmented skin lesions," *Semin. Cutan. Med. Surg.* **22**(1), 9–20 (2003).
8. P. Corcuff, C. Bertrand, and J. L. Leveque, "Morphometry of human epidermis *in vivo* by real-time confocal microscopy," *Arch. Dermatol. Res.* **285**(8), 475–481 (2003).
9. S. el Gammal, R. Hartwig, S. Aygen, T. Bauermann, C. el Gemmal, and P. Altmeyer, "Improved resolution of magnetic resonance microscopy in examination of skin tumors," *J. Invest. Dermatol.* **106**, 1287–1292 (1996).
10. J. Wezel, "Optical coherence tomography in dermatology: a review," *Skin Res. Technol.* **7**, 1–9 (2001).
11. G. B. Jemec, M. Gniadecka, and J. Ulrich, "Ultrasound in dermatology: I. high frequency ultrasound," *Eur. J. Dermatol.* **6**, 492–497 (2000).
12. M. Huzaira, F. Rius, M. Rajadhyaksha, R. R. Anderson, and S. Gonzalez, "Topographic variations in normal skin, as viewed by *in vivo* reflectance confocal microscopy," *J. Invest. Dermatol.* **116**, 846–852 (2001).
13. S. Gonzalez, M. Gill, and A. C. Halpern, "Reflectance Confocal Microscopy of Cutaneous Tumors: an Atlas with Clinical, Dermoscopic and Histological Correlations," Informa Healthcare, London (2008).
14. Z. Matuszak and M. Wasilewska-Radwanska, "Optical properties of melanin solutions, estimation of polymer particles size," *Proc. Symp. Photon. Technol. 7th Framework Program*, **12–14**, 533–537 (2006).
15. I. A. Vitkin, J. Woolsey, B. C. Wilson, and R. R. Anderson, "Optical and thermal characterization of natural (sepia officinalis) melanin," *Photochem. Photobiol.* **59**, 455–462 (1994).
16. G. J. Tearney, M. E. Brezinski, J. F. Southern, B. E. Bouma, M. R. Hee, and J. G. Fujimoto, "Determination of the refractive index of highly scattering human tissue by optical coherence tomography," *Opt. Lett.* **20**, 2258–2260 (1995).
17. M. Rajadhyaksha, M. Grossman, D. Esterowitz, R. H. Webb, and R. R. Anderson, "*In vivo* confocal scanning laser microscopy of human skin: melanin provides strong contrast" *J. Invest. Dermatol.* **104**, 946–952 (1995).
18. R. Langley, M. Rajadhyaksha, P. Dwyer, A. Sober, T. Flotte, and R. Anderson, "Confocal scanning laser microscopy of benign and malignant melanocytic skin lesions *in vivo*," *J. Am. Acad. Dermatol.* **45**, 365–376 (2001).
19. M. Rajadhyaksha, S. Gonzalez, J. Zavislan, R. Anderson, and R. Webb, "*In vivo* confocal scanning laser microscopy of human skin II: advances in instrumentation and comparison with histology," *J. Invest. Dermatol.* **113**, 293–303 (1999).
20. G. Pellacani, M. Vinceti, S. Bassoli, R. Braun, S. Gonzalez, P. Guitera, C. Longo, A. A. Marghoob, S. W. Menzies, S. Puig, A. Scope, S. Seidenari, and J. Malvehy, "Reflectance confocal microscopy and features of melanocytic lesions: an internet-based study of the reproducibility of terminology," *Arch. Dermatol.* **145**(10), 1137–1143 (2009).
21. G. Pellacani, C. Longo, G. Ferrara, A. M. Cesinaro, S. Bassoli, P. Guitera, S. W. Menzies, and S. Seidenari, "Spitz nevi: *In vivo* confocal microscopic features, dermatoscopic aspects, histopathologic correlates, and diagnostic significance," *J. Am. Acad. Dermatol.* **60**(2), 236–247 (2009).
22. S. L. Jacques, J. C. Ramella-Roman, and K. Lee, "Imaging skin pathology with polarized light," *J. Biomed. Opt.* **7**(3), 329–340 (2002).
23. Y. Pan, D. S. Gareau, A. Scope, M. Rajadhyaksha, A. Mulani, and A. Marghoob, "Polarized and nonpolarized dermoscopy," *Arch. Dermatol.* **44**(6), 828–829 (2008).
24. M. Elbaum, "Computer aided melanoma diagnosis," *Dermatol. Clin.* **20**, 735–747 (2002).
25. R. Friedman, D. Gutkowicz-Krusin, M. Farber, M. Warycha, L. Schneider-Kels, N. Papastathis, M. C. Mihm, J. P. Googe, R. King, V. G. Prieto, A. W. Kopf, D. Polsky, H. Rabinovitz, M. Oliviero, A. Cognetta, D. S. Rigel, A. Marghoob, J. Rivers, R. J. M. Grant-Kels, and H. Tsao, "The diagnostic performance of expert dermatologists vs a computer-vision system on small-diameter melanomas," *Arch. Dermatol.* **144**(4), 476–482 (2008).
26. V. Panastii, V. Devirgiliis, M. Curzio, V. Roberti, S. Gobbi, R. Masciagelo, B. Mastrecchia, S. Calvieri, and U. Bottoni, "The reticular point of view in dermatoscopy," *J. Am. Acad. Dermatol.* **61**(4), 605–610 (2009).
27. G. Pellacani, C. Grana, and S. J. Seidenari, "Algorithmic reproduction of asymmetry and border cut-off parameters according to the ABCD rule for dermoscopy," *Eur. Acad. Dermatol. Venereol.* **20**(10), 1214–1219 (2006).
28. B. H. Willis, P. Barton, P. Pearmain, S. Bryan, and C. Hyde, "Cervical screening programmes: can automation help? Evidence from systematic reviews, an economic analysis and a simulation modeling exercise applied to the UK," *Health Technol. Assess.* **9**(13), 1–207 (2005).
29. E. Davey, J. d'Assuncao, L. Irwig, P. Macaskill, S. F. Chan, A. Richards, and A. Farnsworth, "Accuracy of reading liquid based cytology slides using the ThinPrep Imager compared with conventional cytology: prospective study," *BMJ* **335**(7609), 1–2 (2007).
30. Z. Tannous, M. Mihm, T. Flotte, and S. Gonzalez, "*In vivo* examination of lentigo maligna and malignant melanoma *in situ*, lentigo maligna type by near-infrared reflectance confocal microscopy: comparison with *in vivo* images with histologic section," *J. Am. Acad. Dermatol.* **46**, 260–263 (2002).
31. A. Gerger, S. Koller, T. Kern, C. Massone, K. Steiger, E. Richtig, H. Kerl, and J. Smolle, "Diagnostic applicability of *in vivo* confocal laser scanning microscopy in melanocytic skin tumors," *J. Invest. Dermatol.* **137**, 493–498 (2005).
32. D. S. Gareau, G. Merlino, C. Corless, M. Kulesz-Martin, and S. L. Jacques, "Noninvasive imaging of melanoma with reflectance mode confocal scanning laser microscopy in a murine model," *J. Invest. Dermatol.* **127**, 2184–2190 (2007).
33. G. Pellacani, P. Guitera, C. Longo, M. Avramidis, S. Seidenari, and S. Menzies, "The impact of *in vivo* reflectance confocal microscopy for the diagnostic accuracy of melanoma and equivocal melanocytic lesions," *J. Invest. Dermatol.* **127**, 2759–2765 (2007).
34. See <http://www.dangareau.net/MelDetect1/index.html>.
35. K. J. Busam, K. Hester, C. Charles, D. L. Sachs, C. Antonescu, S. González, and A. Halpern, "Detection of clinically amelanotic malignant melanoma and assessment of its margins by *in vivo* confocal scanning laser microscopy," *Arch. Dermatol.* **137**, 923–929 (2001).
36. M. Rajadhyaksha, S. Gonzalez, and J. M. Zavislan, "Detectability of contrast agents for confocal reflectance imaging of skin and microcirculation," *J. Biomed. Opt.* **9**, 323–331 (2004).

37. K. Todak, M. A. Pathak, J. A. Parrish, T. B. Fitzpatrick, and W. C. Quevedo, Jr., "Alteration of racial differences in melanosome distribution in human skin after exposure to ultraviolet light," *Nature [New Biol]* **236**(66), 143–145 (1972).
38. K. J. Busam, A. A. Marghoob, and A. Halpern, "Melanoma diagnosis by confocal microscopy: promise and pitfalls," *J. Invest. Dermatol.* **125**, 1–3 (2005).
39. Y. L. Kim, Y. Liu, R. K. Wali, H. K. Roy, M. J. Goldberg, A. K. Kromin, K. Chen, and V. Backman, "Simultaneous measurement of angular and spectral properties of light scattering for characterization of tissue microarchitecture and its alteration in early precancer," *IEEE. J Sel. Top. Quant.* **9**(2), 234–256 (2003).
40. H. F. Zhang, K. Maslov, and L. V. Wang, "In vivo imaging of subcutaneous structures using functional photoacoustic microscopy," *Nature Protocols* **2**(4), 797–804 (2007).
41. S. Kurgol, J. G. Dy, M. Rajadhyaksha, and D. H. Brooks, "Localizing the dermis/epidermis boundary in reflectance confocal microscopy images with a hybrid classification algorithm," *IEEE Intl. Symp. Biomed. Imag. Nano Macro, ISBI* 1322–1325 (2009).
42. R. R. Anderson and J. A. Parrish, "Optical properties of human skin," *Chap. 6 in The Science of Photomedicine*, J. D. Regan, and J. A. Parrish, Eds., pp. 147–194, Plenum Press, New York (1982).
43. R. L. Olsen, J. Gaylor, and M. A. Everett, "Skin color, melanin, and erythema," *Arch. Dermatol.* **108**, 541–544 (1973).